

## Local structural and compositional determination via electron scattering: Heterogeneous Cu(001)-Pd surface alloy

J. Sun,<sup>1,\*</sup> J. B. Hannon,<sup>2</sup> G. L. Kellogg,<sup>3</sup> and K. Pohl<sup>1</sup>

<sup>1</sup>*Department of Physics, University of New Hampshire, Durham, New Hampshire 03824, USA*

<sup>2</sup>*IBM Research Division, T. J. Watson Research Center, Yorktown Heights, New York 10598, USA*

<sup>3</sup>*Sandia National Laboratories, Albuquerque, New Mexico 87185, USA*

(Received 21 June 2007; published 13 November 2007)

We have measured the structure and chemical composition of ultrathin Pd films on Cu(001) using low-energy electron microscopy. We determine their local stoichiometry and structure, with 8.5 nm lateral spatial resolution, by quantitatively analyzing the scattered electron intensity and comparing it to dynamical scattering calculations, as in a conventional low-energy electron diffraction (LEED)-*IV* analysis. The average *t*-matrix approximation is used to calculate the total atomic scattering matrices for this random substitutional alloy. As in the traditional LEED analysis, the structural and compositional parameters are determined by comparing the computed diffraction intensity of a trial structure to that measured in experiment. Monte Carlo simulations show how the spatial and compositional inhomogeneity can be used to understand the energetics of Cu-Pd bonding.

DOI: [10.1103/PhysRevB.76.205414](https://doi.org/10.1103/PhysRevB.76.205414)

PACS number(s): 68.37.Nq, 61.14.Hg, 68.18.Fg, 68.55.Nq

### I. INTRODUCTION

Ultrathin metal films on metal surfaces can adopt unusual alloy structures with no bulk analog. Understanding the electronic, magnetic, and catalytic properties of these “surface alloys” remains a major challenge in surface physics.<sup>1</sup> One reason for this is that many surface alloy phases are *metastable*, with the equilibrium phase being a dilute random bulk alloy. Metastability can make it difficult to create reproducible, homogeneous alloy films. Also, many surface alloys are structurally inhomogeneous at the nanometer scale. In order to understand quantitatively how film properties are related to structure and ultimately to atomic bonding, structural and compositional heterogeneity must be characterized.

Here, we describe in detail a quantitative analysis of electron diffraction that allows us to determine the local three-dimensional composition and structure of an alloy surface with nanometer-scale spatial resolution. In traditional low-energy electron diffraction (LEED) experiments, diffraction patterns are acquired from a large illuminated area. A quantitative analysis of the diffracted intensity versus electron energy (LEED-*IV*) can be used to determine the *average* composition and structure. We perform a quantitative LEED-*IV* analysis on a low-energy electron microscopy (LEEM) image, which allows us to quantitatively determine the alloy film composition and structure with 8.5 nm lateral spatial resolution. Specifically, we use LEED-*IV* to analyze specularly reflected electrons that are incident normal to the surface. From the energy dependence of their reflectivity, we determine local alloy composition and structure.

In previous work, we used this approach to show that motion of surface steps during growth can make CuPd surface alloy films heterogeneous.<sup>2</sup> Specifically, we showed that mobile Pd in the top two layers of the film is “buried” by advancing steps. Here, we describe additional experiments that demonstrate the accuracy of our technique. In addition, we describe time-resolved alloy profile measurements that support our step-flow overgrowth model. Finally, we present

a detailed analysis of the errors in our concentration profile measurements.

We have applied our technique to the well-known Pd/Cu(001) surface alloy system, one of the most studied metal-on-metal growth systems. When submonolayer coverages of Pd are deposited onto a Cu(001) surface held at temperatures below 173 K, the Pd atoms remain on the surface with a  $1 \times 1$  periodicity.<sup>3</sup> However, if the temperature is raised to room temperature, the Pd atoms exchange with Cu atoms in the first layer, forming a  $c(2 \times 2)$  checkerboard layer. This surface alloy phase has been studied extensively using LEED,<sup>4-6</sup> scanning tunneling microscopy,<sup>7</sup> and electron-energy loss spectroscopy.<sup>8</sup> In a study using positron-induced Auger electron spectroscopy, Koymen *et al.*<sup>3</sup> showed that when the  $c(2 \times 2)$  surface alloy phase is annealed above 423 K, the Pd atoms in the surface layer move to the *second* layer. That is, the  $c(2 \times 2)$  surface alloy becomes covered by a layer of Cu. Barnes *et al.*<sup>9</sup> characterized the formation of this “underlayer”  $c(2 \times 2)$  phase in more detail using LEED. The sequence of phases is shown schematically in Fig. 1.

When Pd incorporates into the surface, the ejected Cu atoms either migrate to steps or coalesce to form new islands. Even when the incident Pd flux is low (2.5 ML/h), significant island nucleation can occur, leading to a highly nonuniform surface. In order to limit island nucleation, we deposited Pd at 473 K and at a very low rate (about 1 ML/h). Under these deposition conditions, we observed significantly reduced island nucleation.

Here, we focus on the underlayer alloy and investigate its structural and compositional development during deposition. Submonolayer Pd is deposited on Cu(001) with a deposition rate of about 1 ML/h at 473 K. Specular *IV* (intensity vs voltage) curves are extracted from LEEM images and analyzed with a dynamical LEED theory (LEED-*IV*). The average *t*-matrix (ATA) method<sup>10,11</sup> is used for the random alloy lattice *t*-matrix calculation. A temporal evolution of the composition on both the uniform terrace and the heterogeneous near-step areas is investigated with a resolution of  $\sim 8.5$  nm.

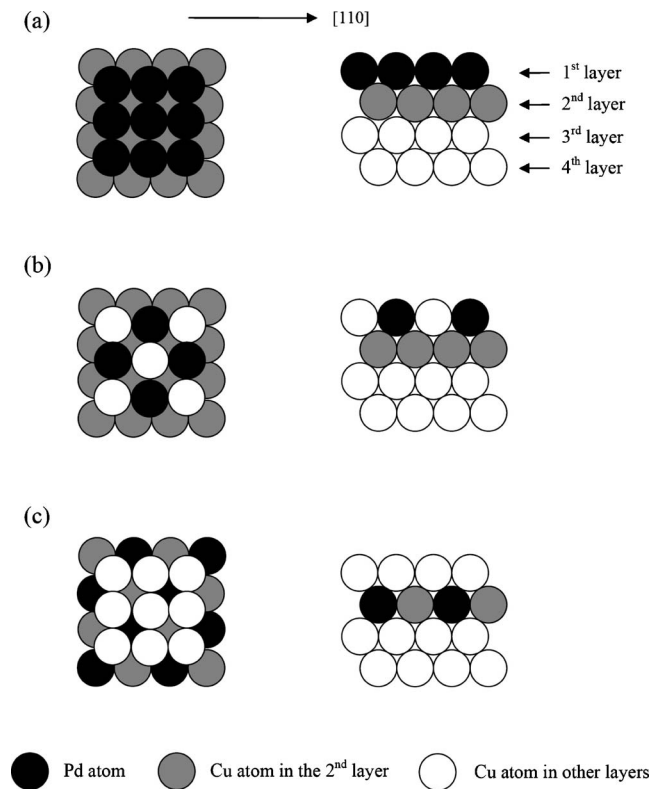


FIG. 1. Top view (left column) and side view (right column) of CuPd surface structures on Cu(001) at different temperatures. (a)  $p(1 \times 1)$  Pd overlayer below 173 K, (b)  $c(2 \times 2)$  overlayer at room temperature, and (c)  $c(2 \times 2)$  underlayer above about 423 K.

Studies on the uniform terrace (i.e., far from steps) show a second layer  $c(2 \times 2)$  intermixing alloy capped by a nearly pure Cu top layer. The Pd concentration far from steps grows more slowly than linear, despite a constant Pd flux of about 0.9 ML/h. Line scan studies across a step show a step-induced heterogeneous structure. Monte Carlo simulations are carried out to determine the laterally equilibrated structure in the first two layers. Results from careful tests on clean Cu(001) surfaces and Cu(001)- $c(2 \times 2)$ -Pd underlayer alloys are compared with previous reports, and an excellent agreement is obtained. The LEEM image intensity analysis proves to be effective for this model system, and generally applicable to surface alloy systems.

The paper is structured as follows. Experimental and computational methods will be presented in Sec. II. Results and discussions from the structural and compositional analysis and the Monte Carlo simulations, including an estimation of the errors, are described in Sec. III. Section IV concludes this paper with a summary.

## II. METHODS

### A. Experiment

LEEM is a unique electron imaging technique that can be used to investigate surface processes, such as thin film growth, surface etching, and adsorption.<sup>12,13</sup> In our experi-

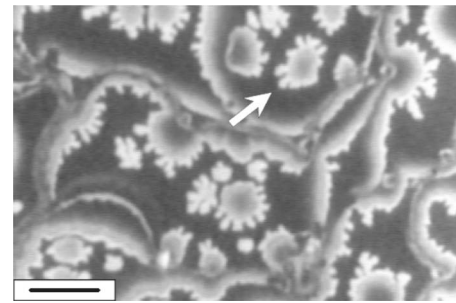


FIG. 2. 13.1 eV LEEM image after a deposition of  $\approx 0.6$  ML Pd on Cu(001) at 473 K. The image shows dendritic islands (one indicated by an arrow) and significant contrast variation near steps. Scale bar: 1  $\mu\text{m}$ .

ments, we use this technique to image the growth of the CuPd surface alloy *in situ* during Pd deposition onto Cu(001) using a commercial Knudsen cell. In LEEM, an image is formed from low-energy electrons (10–100 eV) reflected from the surface. In the imaging conditions we employed, both the incident and reflected beams are normal to the surface, as in conventional LEED. We place an aperture in the optical path so that only electrons in the specular beam [the (00) LEED beam] contribute to the image. Thus, the LEEM image intensity measures the spatial variation of the (00) beam at a particular energy. By recording images at different beam energies, the dependence of the intensity on the beam energy (the LEED-*IV* curve) can be recorded for any point on the surface. In this way, we measure the time evolution of the Pd concentration of the film with a spatial resolution of 8.5 nm and a time resolution of about 3 min. When the aperture is removed, we can record *IV* curves for different beams by imaging the diffraction plane, as in conventional LEED.

It is well known that reduced surface mass transport can give rise to island nucleation that makes the surface alloy phase inhomogeneous and rough.<sup>7,14</sup> In order to reduce island nucleation and produce a structure closer to equilibrium, we deposit Pd at a very slow rate (2.5 ML/h), with the Cu(001) substrate held at 473 K. A LEEM image recorded using 13.1 eV electrons after the deposition of about 0.6 ML Pd is shown in Fig. 2. Its most striking feature is the spatial variation of the contrast. The steps and island edges appear brighter than regions on the terrace. Small islands are uniformly bright. This image shows that the alloy film is inhomogeneous even when the flux is low and the deposition is carried out at elevated temperatures. The inhomogeneity is clearly associated with the presence of atomic steps. A recent LEED analysis of a similarly grown film suggests that the Pd is located primarily in the second layer, in a  $c(2 \times 2)$  structure, while the surface consists almost entirely of Cu.<sup>9</sup>

If the deposition is carried out with an even lower flux, island nucleation is further suppressed. A sequence of LEEM images recorded during a deposition with a flux of 1.0 ML/h is shown in Fig. 3. The images in column (a) were recorded using 13.5 eV electrons, and those in column (b) with 20.1 eV electrons. As more Pd is deposited, ejected Cu atoms diffuse to the steps, causing them to move. Far from the

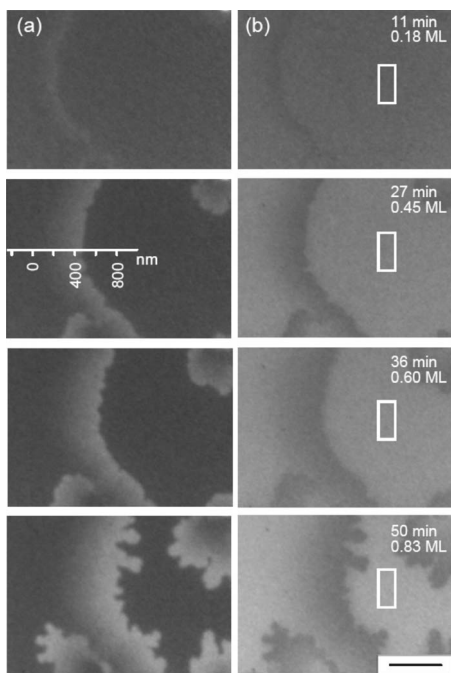


FIG. 3. Sequence of LEEM images recorded during the deposition of Pd on Cu(001) at 473 K. The electron beam energy was 13.5 eV for the images in column (a) and 20.5 eV for the images in column (b). The images are labeled by the elapsed deposition time and the total Pd coverage. The marked line in column (a) is used for the near-step heterogeneous structure study. The rectangular area in column (b) is used for the uniform structure study on the terrace. Scale bar: 500 nm.

steps, the image intensity is uniform. However, at the upper side of the step, the image intensity is spatially inhomogeneous.

### B. Quantitative analysis of low-energy electron microscopy intensity data

In a LEED-*IV* analysis, *IV* curves are calculated for a trial structure and compared with experiment. The parameters of the trial structure, in this case the structure and alloy composition in the first three surface layers, are varied to give the best agreement with the measured *IV* curve. We use a dynamical LEED-*IV* analysis to determine a near-surface structure and composition from electron reflectivity data acquired using LEEM. To calculate the *IV* curves, we used computer codes from Adams *et al.*<sup>15–17</sup> which were developed from the programs of Pendry<sup>18</sup> and Van Hove and Tong.<sup>19</sup> The codes simultaneously optimize both structural and nonstructural parameters, and have been tested extensively for Al(110), Al(100)-*c*(2×2)-Li, Al(111)-(2×2)-Na,<sup>17</sup> and Bi(111).<sup>20</sup> Up to 13 phase shifts<sup>21</sup> ( $L=12$ ) are used for the atomic *t*-matrix calculation. The average *t*-matrix approximation method is used for the random alloy lattice. For this CuPd binary alloy, an effective *t*-matrix  $\bar{t}$  is calculated as  $\bar{t} = xt_{\text{Pd}} + (1-x)t_{\text{Cu}}$ , where  $x$  is the Pd concentration and,  $t_{\text{Pd}}$  and  $t_{\text{Cu}}$  are individual *t* matrices for pure Pd and Cu systems. A  $\chi^2$ -based  $R_2$  factor is employed to measure the agreement

level between the experimental and theoretical data.<sup>17</sup> Here, we show that this approach gives accurate results for both the clean Cu(001) surface as well as for the Pd/Cu(001) structures analyzed previously with conventional LEED-*IV*. Three key differences between LEEM and conventional LEED-*IV* are of particular concern in our analysis: (1) the relatively low electron kinetic energy in LEEM compared to LEED, (2) the limited electron kinetic energy range in our LEEM experiments, and (3) the proper treatment of the inelastic background.

The electron kinetic energy in our LEEM experiments (10–100 eV) is lower than that typically used in LEED *IV* (50–500 eV). This complicates the quantitative analysis because, within about 50 eV of the vacuum level, the mean-free path of electrons in solids is strongly energy dependent.<sup>22</sup> Consequently, in calculations of the electron reflectivity, the inelastic damping potential (i.e., the imaginary part of the inner potential  $V_{im}$ ) cannot be assumed to be constant as in the conventional LEED-*IV* analysis. After evaluating various proposed models for the imaginary part of the inner potential, we found that  $V_{im}(E) = V_{damp}E^{1/3}$  consistently gave the best agreement between the measured and calculated *IV* curves for clean Cu(001). Demuth *et al.*<sup>23</sup> used this exponential form for low-index surfaces of Ni for energies in the range of 10–220 eV. In addition, Noonan *et al.*<sup>24</sup> and Davis and Noonan<sup>25</sup> used this form for both Cu(110) and Cu(001). We optimized the constant prefactor  $V_{damp}$  as an independent nonstructural parameter in our calculations (see Table I). For the real part of the inner potential  $V_0(E)$ , we used the form proposed by Rundgren,<sup>26</sup> specifically for Cu(001) (in units of eV),

$$V_0(E) = \begin{cases} -13.4 & \text{for } E \leq 36 \text{ eV} \\ -3.6 - 65.8/\sqrt{E+10.0} & \text{for } E > 36 \text{ eV}. \end{cases} \quad (1)$$

This correction to the real part of the inner potential resolved a controversial claim of an in-plane contraction reported in a recent LEED-*IV* study on Cu(001).<sup>27</sup> We include an overall additive constant ( $\Delta V_0$ ) to Eq. (1) as an independent nonstructural parameter in our optimization (see Table I). These energy-dependent inner potential models are the most suitable approximation we can use for our system, and they proved to describe the surface alloy very well.

LEEM images contain a contribution from inelastically scattered and secondary electrons. This contribution can be measured directly by integrating the background intensity near the (00) diffraction spot in the diffraction mode. The inelastically scattered electrons are dispersed out of the optical path by the LEEM prism, so their contribution to the image intensity decreases rapidly with increasing beam energy. We find that the background in our images is approximately proportional to  $\exp(-E/30)$ , where  $E$  is the electron kinetic energy in eV.

## III. RESULTS AND DISCUSSIONS

### A. Low-energy electron diffraction analysis of clean Cu(001)

We tested our treatment of low-energy electrons by analyzing LEEM data recorded in the “diffraction mode.” In this

TABLE I. Optimum parameter values for Cu(001) at 473 K. Interlayer spacings between the  $i$ th and the  $j$ th layer are denoted as  $d_{ij}$ . Root-mean-square vibrational amplitudes for atoms in the  $i$ th layer are denoted as  $u_i$ .  $V_{damp}$  is the prefactor of the imaginary part of inner potential.  $\Delta V_0$  is the overall shift of the real part of the inner potential to Eq. (1).  $c$  is the global scaling constant from beam to beam.  $d^b$  is the corresponding interlayer spacing of the truncated bulk at 473 K.  $\Theta_D$  is the Debye temperature calculated from  $u_i$ .

Parameters	Starting values	Optimized values	$\Delta d/d^b$ (%)			$\Theta_D$ (K)
			This work	Ref. 25	Ref. 28	
$d_{12}$ (Å)	1.811	$1.78 \pm 0.016$	$-1.6 \pm 0.9$	$-1.0 \pm 0.4$	-1.2	-2.4
$d_{23}$ (Å)	1.811	$1.83 \pm 0.033$	$+1.0 \pm 1.8$	$+1.7 \pm 0.6$	+0.9	+0.9
$u_1$ (Å)	0.182	$0.27 \pm 0.020$				$213_{-15}^{+17}$
$u_2$ (Å)	0.182	$0.19 \pm 0.017$				$300_{-25}^{+30}$
$V_{damp}$	0.80	$0.92 \pm 0.07$				
$\Delta V_0$ (eV)	0.00	$1.02 \pm 0.31$				
$c$	198.7	$121.3 \pm 22.2$				
$R$ factor	0.647	0.038				

mode, we record spatially averaged diffraction patterns, just as in conventional LEED. A typical diffraction image from Cu(001) is shown in Fig. 4. The  $IV$  curves of three symmetry in-equivalent beams (00), (10), and (11) from clean Cu(001) measured in this way are shown in Fig. 5. The Debye temperature of the bulk is fixed at 315 K, while the vibrational amplitudes for the first two layers are optimized.

A direct comparison of the computed and measured  $IV$  curves is given in Fig. 5. The agreement is excellent. The inclusion of an energy-dependent  $V_0$  greatly improves the agreement in the peak positions. The energy-dependent  $V_{im}$  is essential in reproducing the relative peak intensities, especially at low energies. The best-fit structural parameters for clean Cu(001) are summarized in Table I. The error bars in the clean surface analysis are based on an increase of 4% in the  $R_2$  factor.<sup>17</sup> We find a contraction of 1.6% in the first interlayer spacing and an expansion of 1.0% in the second in contrast to the bulk interlayer spacing of 1.811 Å. The Debye temperatures for the first two top layers are found to be lower than the bulk, characteristic of larger atomic vibrational amplitudes at the surface. The results agree very well

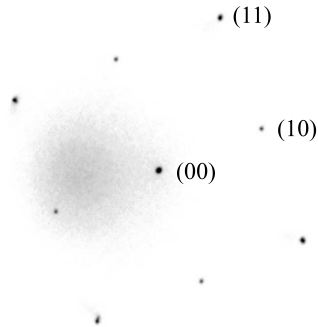


FIG. 4. Diffraction pattern for clean Cu(001) at 46.2 eV measured in the LEEM. The diffuse intensity in the left of the image is due to secondary electrons, which are not filtered out of the image.

with previous investigations by LEED- $IV$ ,<sup>25</sup> spin-polarized LEED,<sup>28</sup> and medium-energy ion scattering.<sup>29</sup>

### B. Low-energy electron microscopy analysis of clean Cu(001)

Next, we compare the  $IV$  spectra of the (00) beam extracted in both LEED and LEEM modes, and perform a structural analysis solely based on the latter. The measured LEEM image intensity (solid curve) from clean Cu(001) at 313 K, as a function of electron kinetic energy, is shown in Fig. 6 together with the  $IV$  curve measured in the diffraction mode (dash-dotted curve). The inelastic background, described above, has been subtracted from the solid curve. The agreement is very good, demonstrating the equivalence of measuring the (00) peak intensity in either the LEEM or the LEED mode.

We have performed a structural analysis using only data from the (00) beam up to 250 eV. We find a good agreement between the computed (dashed curve) and measured  $IV$  curves. Specifically, we find  $d_{12} = -1.6 \pm 0.9\%$ , and  $d_{23} = +1.5 \pm 2.0\%$ , with an  $R_2$  factor of 0.051. These results agree well with previous investigations summarized in Table I. It shows that the (00)  $IV$  curve contains enough information, even over a limited energy range, to perform an accurate structural analysis.

### C. Low-energy electron microscopy analysis of Cu(001)- $c(2 \times 2)$ -Pd

The analysis of clean Cu(001) shows that data from the (00) beam are sufficient to determine the surface structural parameters, i.e., the interlayer spacings. We tested our ability to determine layer-resolved Pd concentrations by analyzing a known alloy structure: the Pd/Cu(100) alloy phase prepared by depositing 0.6 ML of Pd on Cu(001) at 473 K. Again, in our analysis, we include only data from the (00) beam over an energy range of 10–100 eV. To reduce noise, we averaged the image intensity over the boxed region indicated in

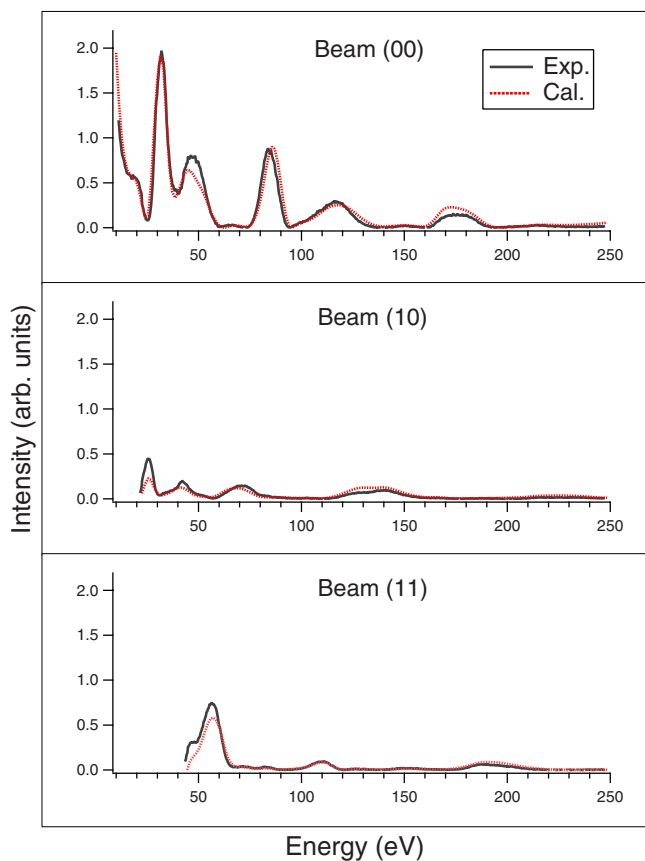


FIG. 5. (Color online) Measured (solid) and best-fit calculated (dotted) IV curves for clean Cu(001) at 473 K. The same scaling factor is used for all three beams.

Fig. 3. It is clear from the images that the intensity (and structure) is homogeneous far from the step. This same procedure cannot be used near the step, where the intensity is spatially inhomogeneous. The basic structure of this phase was determined using conventional LEED-IV by Barnes *et al.*,<sup>9</sup> who deposited Pd at room temperature until the  $(1/2, 1/2)$  beam intensity reached a maximum, followed by annealing at 550 K. According to the early work by Pope *et al.*,<sup>30</sup> the maximum  $(1/2, 1/2)$  beam intensity occurs at a Pd coverage of  $0.55 \pm 0.10$  ML. Barnes *et al.* showed that upon annealing, almost all of the Pd migrates to the second layer in a  $c(2 \times 2)$  alloy structure.

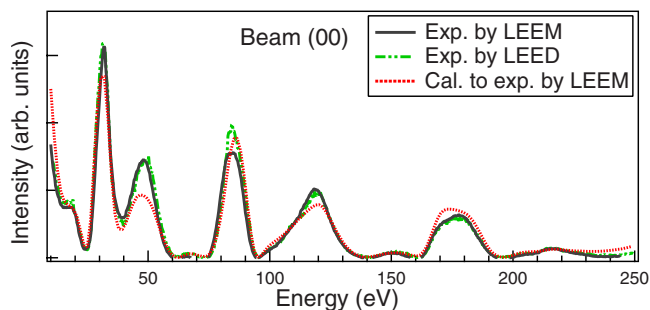


FIG. 6. (Color online) Comparison between the (00) beam intensity measured in LEEM (solid), LEED (dash-dotted), and the best fit (dotted) to the LEEM curve.

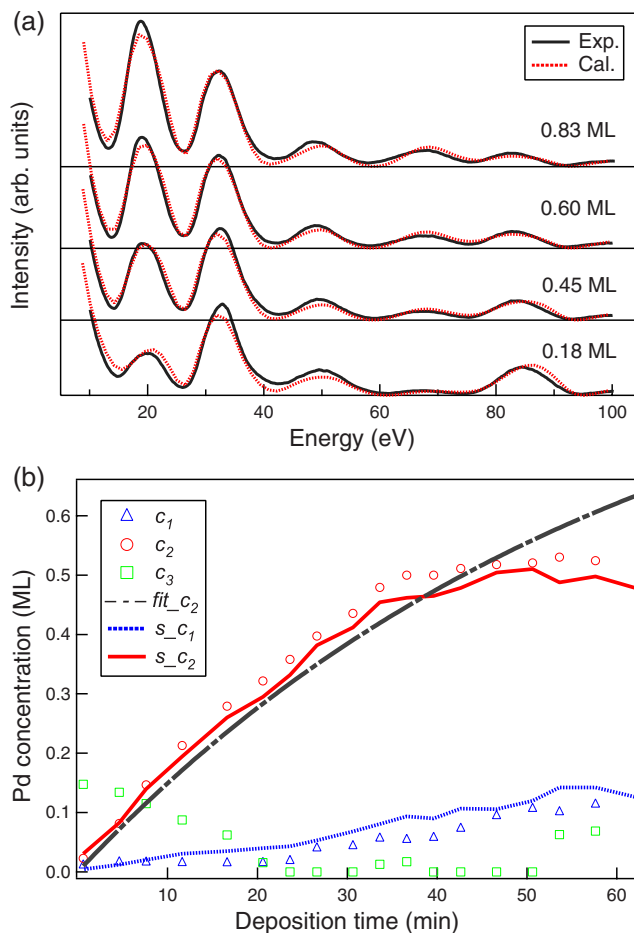


FIG. 7. (Color online) Analysis of the Pd concentration on the terrace (averaged over the white rectangle in Fig. 3). (a) Measured (solid) and computed (dotted) image intensity as a function of electron beam energy at four different Pd coverages. (b) Corresponding time evolution of the Pd concentrations  $c_i$  ( $i=1,2,3$ ) for the first three surface layers.  $fit\_c_2$  is the fitting curve of  $c_2$  according to Eq. (2) with a flux of 0.9 ML/h.  $s\_c_1$  and  $s\_c_2$  are simulated uptake curves for  $c_1$  and  $c_2$ .

Our LEEM intensity data for this phase are shown as the 0.60 ML curve (solid) in Fig. 7(a). In our analysis, each of the three topmost layers is divided into two  $c(2 \times 2)$  checkerboard sublattices. The ATA method is used to calculate random alloy  $t$  matrices for each sublattice. Independently optimized compositional parameters are  $\theta_{11}$  and  $\theta_{12}$ ,  $\theta_{21}$  and  $\theta_{22}$ ,  $\theta_{31}$  and  $\theta_{32}$ , representing the Cu concentration (in monolayers) in each of the two sublattices of the first, the second, and the third layer, respectively. Note that we make no assumption about the total amount of Pd in the film. All of these parameters are allowed to vary within an interval of 0 to 1 ML at a step of 0.001 ML during optimization. The Pd concentration in the  $i$ th layer,  $c_i$ , is given by  $c_i = 1 - (\theta_{i1} + \theta_{i2})/2$ , ( $i=1,2,3$ ). A value of 0.86 for  $V_{damp}$  is used for this structure. Debye temperatures for all layers are fixed at the bulk value, i.e., 315 K for Cu and 275 K for Pd. We did not optimize the Debye temperature but simply tested different values and found no significant structural changes. The best-fit values of the main parameters are shown in Table II,

TABLE II. Comparison of results for this work with that of Barnes *et al.* (Ref. 9) for the Cu(001)- $c(2 \times 2)$ -Pd alloy.  $d_{12}$  and  $d_{23}$  are the first and the second interlayer spacing, respectively.  $\theta_{11}$  and  $\theta_{12}$ ,  $\theta_{21}$  and  $\theta_{22}$ , and  $\theta_{31}$  and  $\theta_{32}$ , representing the Cu concentration in each of the two sublattices of the first, the second, the third layer, respectively.  $c_1$ ,  $c_2$ , and  $c_3$ , the Pd concentration for the three top-most layers,  $c_i = 1 - (\theta_{i1} + \theta_{i2})/2$ , ( $i=1,2,3$ ).  $z_2$  and  $z_4$  are the rippling of sublattices in the second layer and in the fourth layer, respectively.

Parameters	This work	Ref. 9
$d_{12}$ (Å)	1.85	1.86
$d_{23}$ (Å)	1.85	1.85
$\theta_{11}$ (ML)	1.00	
$\theta_{12}$ (ML)	0.89	
$c_1$ (ML)	0.06	Fixed at 0
$\theta_{21}$ (ML)	1.00	
$\theta_{22}$ (ML)	0.04	
$c_2$ (ML)	0.48	Fixed at 0.5
$\theta_{31}$ (ML)	0.97	
$\theta_{32}$ (ML)	1.00	
$c_3$ (ML)	0.02	Fixed at 0
$z_2$ (Å)	0.05	0.07
$z_4$ (Å)	Fixed at 0	0.2
R factor	0.009	0.28 ( $R_p$ )

which are in excellent agreement with those found by Barnes *et al.*<sup>9</sup> Specifically, we find that the Pd resides entirely in one sublattice in the second layer. This is in agreement with the checkerboard model. The bulk interlayer spacings used in this work and in Ref. 9 are 1.811 and 1.805 Å, respectively.  $z_2$  and  $z_4$  are the rippings of the sublattices in the second layer and in the fourth layer, respectively. The value of rippling in the second layer indicates a small upward shift of the Cu sublattice normal to the surface due to size difference between Cu and Pd atoms. In our work,  $z_4$  is not optimized, while in Ref. 9 a significant rippling of 0.2 Å in  $z_4$  was reported. However, *ab initio* modeling<sup>31</sup> does not support substantial rippling in the fourth layer. A comparison between the measured and computed *IV* spectra is shown in Fig. 7(a).

In conclusion, an excellent agreement between experimental and calculated (00) beam *IV* curves has been obtained for both clean Cu(001) as well as for a known Pd/Cu(001) underlayer alloy structure. The structural parameters derived from our analysis agree well with those determined using conventional LEED. Notably in the underlayer alloy case, we get consistent results even without a large buckling in the fourth layer. These results give us confidence that our analysis is capable of determining surface structural and compositional parameters for Pd/Cu(001) structures with high accuracy.

#### D. Temporal evolution of Pd on Cu(001) on terrace

Figure 3 shows a sequence of LEEM images recorded during the deposition of Pd with a flux of 1.0 ML/h. The

images in columns (a) and (b) are recorded at 13.5 and 20.1 eV beam energies, respectively. There is an atomic step running vertically near the center of the images. As Pd is deposited, the step moves to the right due to the attachment of ejected Cu atoms. As growth proceeds, the contrast variation in the image increases. The step profile is initially smooth, but becomes wavy as the amount of Pd in the surface region increases. A quantitative analysis of the image intensity, described below, shows that the image appears bright at 20.5 eV when significant amounts of Pd reside in the second layer. At 13.5 eV, the image appears bright when the amount of Pd in the third layer is large. Thus, the images in column (a) show qualitatively how the amount of Pd in the third layer evolves with time while those in column (b) show how the second layer evolves. The images show directly that the Pd concentration is uniform on the terrace, but is highly inhomogeneous at the upper side of atomic steps. The evolution of the alloy composition can be determined quantitatively by analyzing the full *IV* curves at each point on the surface with a resolution of  $\sim 8.5$  nm. We do this by acquiring images while the electron beam energy is swept from 10 to 100 eV. The heterogeneous structure has been found to be induced by step flow<sup>2</sup> and will be further described in the next section.

Here, we describe the analysis of the uniform areas on the terrace far from steps. *IV* curves from the terrace at four different Pd coverages, i.e., deposition times, are shown in Fig. 7(a). The *IV* data were obtained by averaging over a local rectangular homogeneous region indicated in Fig. 3. The most obvious change in the *IV* curve with increasing Pd coverage is the growth of the peak around 20 eV. The evolution of the composition of the film can be determined by comparing the measured *IV* curves to electron scattering calculations as in conventional LEED. Using the procedure outlined in the preceding section, we determine the Pd concentration in each of the first three surface layers. We recorded *IV* curves at 3 min intervals; thus, we can determine the evolution of the Pd coverage with a 3 min time resolution. The results of this analysis are shown in Fig. 7(b), where the Pd concentrations in the surface ( $c_1$ ), second ( $c_2$ ), and third ( $c_3$ ) layers, far from steps, are shown as a function of time. The analysis shows that  $c_2$  grows monotonically with time, while  $c_1$  and  $c_3$  are both small and essentially constant. The small value of  $c_3$  suggests that a direct migration of Pd from the second layer to the third is slow, even at 473 K. If the Pd atoms were evenly distributed on the terrace during growth, the total Pd concentration,  $c_1 + c_2 + c_3$ , would grow linearly with time, which it does not. It appears that while the Pd concentration on the terrace is laterally equilibrated (i.e., with uniform image intensity), some of the incident Pd flux is lost from the terrace. Previously, we showed that some Pd from the terrace is irreversibly buried by the advancing step.<sup>2</sup> Here, we show that the same step-flow model describes how the concentration of Pd on the terrace develops with time. We assume that there is a constant flux  $F$  of Pd incident onto the surface. Under our deposition conditions at an elevated temperature (473 K), Pd deposited onto the surface migrates preferentially to the second layer. For simplicity, we assume that *all* of the deposited Pd initially goes to the second layer and that migration to other layers does not occur ( $c_1 = c_3$

=0). We further assume that surface mass transport is fast and that, consequently, the Pd concentration in the second layer,  $c_2$ , is spatially uniform. As the step advances during growth, Pd in the second layer in front of the advancing step is converted into *third-layer* Pd trailing the step. In this simplified scenario, the time evolution of  $c_2$  far from a step is given by

$$c_2 = 1 - \exp(-Ft). \tag{2}$$

The dash-dotted curve in Fig. 7(b) shows a fit to Eq. (2) corresponding to  $F=0.9$  ML/h. The fit agrees reasonably well with the LEED analysis, suggesting that the sub-linear growth in the total Pd coverage with time is consistent with burying of Pd by the advancing step. Because the small increase in  $c_1$  with time is ignored, fitting to  $c_2$  alone underestimates the true flux. If it is assumed that both  $c_1$  and  $c_2$  are buried by the step, i.e., if one overestimates the amount of Pd lost to step overgrowth, a value of  $F=1.1$  ML/h is obtained. In the following, we assume  $F=1.0$  ML/h, a value consistent with the observed step motion during growth.

### E. Composition profiles near a step

A series of LEEM images recorded during Pd growth is shown in Fig. 3. Each image is labeled by the deposition time and total Pd coverage. During the growth, we periodically ramped the energy from 10 to 100 eV. From these data, we construct  $IV$  curves for each point in the image with a time resolution of about 3 min. For each  $IV$  curve, we can perform a full dynamical LEED analysis to determine the *local* structural parameters and layer-resolved Pd concentration (i.e., in each individual image pixel). These data allow us to determine how the three-dimensional Pd concentration evolves with time. It is clear that the image contrast is heterogeneous at the upper side of the step. In Fig. 8, we show how the Pd concentration evolves along the line indicated in Fig. 3. The four panels show the Pd concentrations (along the same line) at four different deposition times.

The most striking feature of the concentration profiles is the asymmetry in the third-layer Pd concentration,  $c_3$ . In front of the advancing step (i.e., at large  $x$ ),  $c_3$  is essentially zero. However, at the trailing side of the step,  $c_3$  is large at the step position but decays monotonically away from it (i.e., toward  $x=0$ ). With time, the amount of Pd at the step edge grows. Previously, we showed that Pd reaches the third layer via step overflow growth.<sup>2</sup> That is, the advancing step turns Pd in the second layer into essentially immobile Pd in the third layer.

A more subtle feature of the concentration profiles is the apparent correlation between the second-layer concentration ( $c_2$ ) and the third-layer concentration ( $c_3$ ). Wherever  $c_3$  is large,  $c_2$  is relatively small. In our earlier work, we used Monte Carlo simulations to show that the heterogeneity in the third layer leads to heterogeneity in the second layer and that the first two layers are laterally equilibrated. The simulation details will be described below.

### F. Monte Carlo simulations

In the simple model outlined above, we assumed that all of the deposited Pd migrates to the second layer and that the

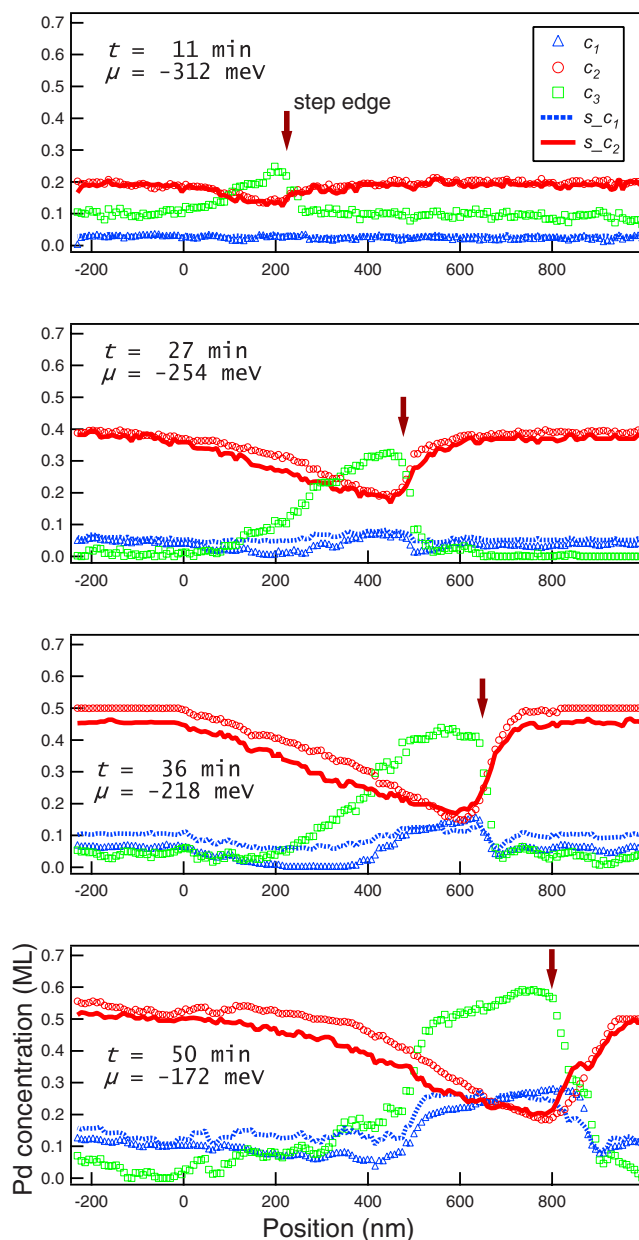


FIG. 8. (Color online) Measured Pd concentration profiles across an advancing step and equilibrated concentration distributions in the first two layers from Monte Carlo simulations.  $c_i$  ( $i=1,2,3$ ) are measured data for the  $i$ th layer.  $s\_c_i$  ( $i=1,2$ ) are the simulated profiles. Each panel corresponds to one deposition time. The chemical potential  $\mu$  is shown and  $\epsilon=-25$  meV. The arrows point to the step edge position.

Pd from the terrace eventually becomes buried by the advancing step. In previous work, we described a more realistic model based on the energetics of Pd-Cu bonding. As we show below, this model can be used to predict the *time evolution* of the Pd concentration profiles, in each layer, both on the terrace and in the heterogeneous regions near the step.

The central premise of the model is that Cu-Pd nearest-neighbor (NN) bonds are favored. This idea is motivated by the stability of the  $c(2 \times 2)$  structure, which contains only Cu-Pd NN bonds and is supported by first-principles

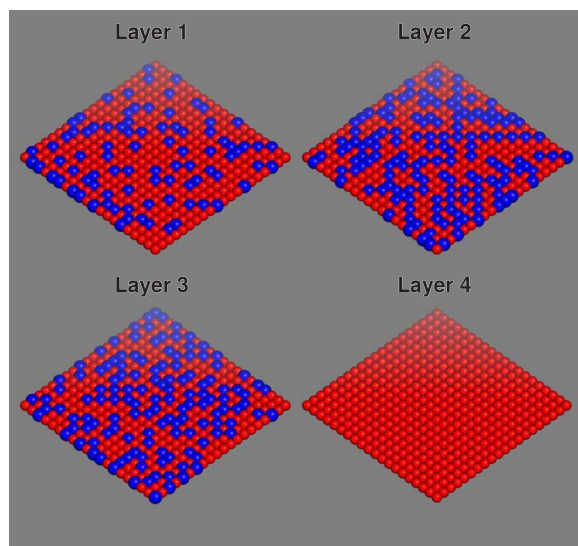


FIG. 9. (Color online) The computed equilibrium structure of an alloy with  $c_1+c_2=0.58$ ,  $c_3=0.33$ , and  $\epsilon=-25$  meV. Cu atoms are shown as lighter balls (red online), Pd atoms as darker balls (blue online).

calculations,<sup>32</sup> empirical modeling,<sup>8</sup> as well as embedded-atom method calculations,<sup>33</sup> which showed that Cu-Pd NN bonds are favored over both Cu-Cu and Pd-Pd bonds. In the Monte Carlo simulations, the internal energy of the film is equal to  $\epsilon N$ , where  $\epsilon$  is the energy of one Cu-Pd NN bond and  $N$  is the number of such bonds.  $\epsilon$  is negative, so the system adopts a structure that favors Cu-Pd nearest neighbors. The simulations were carried out on four-layer slabs with  $20 \times 20$  atoms in each layer with periodic boundary conditions. The atoms in both the third and fourth layers are fixed. The Metropolis algorithm<sup>34</sup> is used to determine the equilibrium distribution of Pd atoms in the film.

In the Monte Carlo simulations of the temporal evolution of the concentrations on the terrace, we compute the values of  $c_1$  and  $c_2$  as a function of total coverage, while  $c_3$  is fixed at the measured value. That is, we compute how a given total coverage on the terrace,  $c_1+c_2$ , is partitioned between the first and second layers, while the Pd coverage in the third layer is fixed. This is a constant- $NVT$  simulation in which we treat the system as a canonical ensemble.<sup>35</sup> A trial move in this simulation involves atom-identity exchange within the first two layers. Simulated results are shown in Fig. 7(b).  $s_{c_1}$  and  $s_{c_2}$  are simulated Pd concentration uptake curves for the first and the second layer. The agreement with experimental data is good, showing that the simple model quantitatively predicts both the spatial and the temporal evolution of the alloy composition. In this simulation,  $\epsilon$  is obtained as  $-25$  meV. An example of a simulated equilibrium structure is shown in Fig. 9 for  $c_1+c_2=0.58$  and  $c_3=0.33$ .

For the heterogeneous surface region near a step, we performed Monte Carlo simulations to predict the equilibrium distribution of Pd within a grand-canonical ensemble frame, a so-called constant- $\mu VT$  simulation. The Pd concentration in the first two layers is determined by the chemical potential,  $\Delta\mu = \mu_{\text{Pd}} - \mu_{\text{Cu}}$ , where  $\mu_{\text{Pd}}$  and  $\mu_{\text{Cu}}$  are the chemical potentials of Pd and Cu, respectively. A trial move in this simu-

lation consists of swapping an atom from one of the first two layers of the slab with an atom from a reservoir in which the Pd chemical potential is  $\mu$  (the Cu chemical potential is 0), while the third-layer concentration is fixed at the experimental value. These rules effectively allow Pd to migrate between the first and second layers of the film, but not to penetrate further into the bulk. When the physical properties of this surface slab are stable, which indicates that it is in equilibrium with the reservoir, we get an average of the total first two-layer concentrations of  $c_1+c_2$  and, simultaneously, the partition of  $c_1$  and  $c_2$  as functions of varying  $c_3$  and  $\mu$ . By matching simulated and experimental total concentrations of  $c_1+c_2$ , we get  $\mu$  for each point along the scan line and  $c_1$  and  $c_2$  as well. Simulation results are shown as  $s_{c_1}$  and  $s_{c_2}$  in Fig. 8, which agree well with the measured profiles, considering this is a highly simplified model. The chemical potentials obtained for 11, 27, 36, and 50 min are  $-312 \pm 0.4$ ,  $-254 \pm 0.9$ ,  $-218 \pm 2.1$ , and  $-172 \pm 1.2$  meV, respectively, and  $\epsilon = -25$  meV throughout. The small deviation in chemical potentials along each scan line demonstrates that the first two layers are laterally well equilibrated and the second layer heterogeneity is caused by the heterogeneity in the third layer. The same conclusion can be reached by calculating the Helmholtz free energy from a thermodynamic integration over temperature<sup>35</sup> and, subsequently, the chemical potential by the derivative of the free energy with respect to the number of Pd atoms. Both fundamentally different methods result in the same chemical potential values. Thus, we have shown that during growth, the Pd concentration in the first two surface layers is laterally equilibrated. A remarkably simple model of the energetics can therefore predict the concentration profiles over the entire surface.

### G. Error analysis in low-energy electron microscopy intensity calculations

We have investigated the reliability of our results by analyzing how the agreement between the measured and computed  $IV$  curves change when  $c_1$ ,  $c_2$ , and  $c_3$  are varied. Statistical  $R$ -factor methods used in conventional LEED- $IV$  are not applicable because of the limited energy range of the data. Instead, we focus on the residual  $|\Delta I(E)|^2$ , defined as the square difference between the computed and measured  $IV$  curves at energy  $E$ . We determine the error bars in the concentrations by varying  $c_1$ ,  $c_2$ , and  $c_3$  until the agreement between the measured and calculated  $IV$  curves becomes noticeably worse (examples are shown in Fig. 10). Our definition of “noticeably worse” corresponds to an increase in the  $R_2$  factor of about 0.015. Using this procedure, we find that the errors in  $c_2$  and  $c_3$  are larger than that in  $c_1$ . Contour plots in Fig. 10 show how the  $R_2$  factor depends on  $c_2$  and  $c_3$  for three different Pd configurations, i.e., at three different points,  $A$ ,  $B$ , and  $C$ , on the line across a step shown in Fig. 3, column (a). To get a more general assessment of the errors, we choose these three typical points with different ratios  $c_2/c_3$ . These three points  $A$ ,  $B$ , and  $C$  correspond to three positions in the line scans: 315 nm at  $t=27$  min, and 660 and 315 nm at  $t=50$  min, respectively.

Three  $IV$  curves are shown at the bottom of each panel:

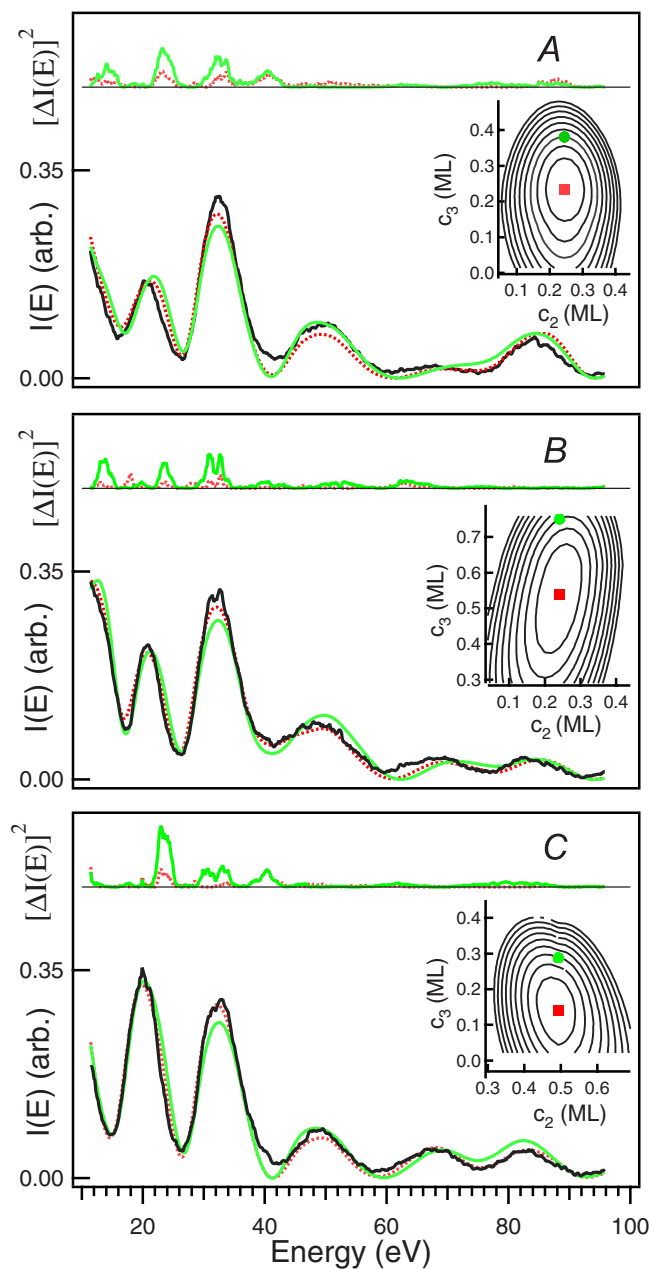


FIG. 10. (Color online) Determination of errors in  $c_2$  and  $c_3$ . *IV* curves at three positions on the line across a step (A, B, and C) are shown at the bottom of each panel. The measured curve is shown as a dark solid line (black online), the best-fit curve is shown as a dotted line, and a computed curve with a worse fit is shown as a gray solid line (green online). The residual  $|\Delta I(E)|^2$  is shown on the top of each panel. The dotted ones are for best-fit data and the solid curves for worse-fit data. The contour plots in the upper right corner of each panel show  $R_2$  as a function of  $c_2$  and  $c_3$ . The solid square indicates the values of  $c_2$  and  $c_3$  for the best-fit point, and the solid circle marks the values for the worse fit. The increment in the  $R_2$  contours is 0.005.

the experimental (darker solid curve), best-fit computed (dotted curve), and one curve (gray solid curve or green online) calculated at a value of  $c_3$  that produced a significantly worse agreement with the measured curve (i.e., with a larger  $R_2$

TABLE III.  $c_2$ ,  $c_3$ , and  $R_2$  factor with error bars at three points on the surface near a step.

Point	Best-fit values		
	$c_2$ (ML)	$c_3$ (ML)	$R_2$ factor
A	$0.25 \pm 0.10$	$0.23 \pm 0.15$	$0.025 + 0.015$
B	$0.24 \pm 0.10$	$0.54 \pm 0.21$	$0.008 + 0.015$
C	$0.49 \pm 0.09$	$0.14 \pm 0.15$	$0.010 + 0.015$

factor). The agreement can be assessed visually by comparing the residual  $|\Delta I(E)|^2$  for the best-fit data (dotted) and worse-fit curves (solid) shown at the top of each panel. The residual for the worse-fit curve is clearly larger than that of the best-fit curve. The contour plots on the right show the dependence of the  $R_2$  factor on  $c_2$  and  $c_3$  near the optimized values. The solid square marks the best-fit values of  $c_2$  and  $c_3$ , while the solid circle indicates those of the worse-fit curve. The increment in the  $R_2$ -factor contours is 0.005. From the elongated shape of the contours, it is clear that the error in  $c_3$  is larger than the error in  $c_2$ . The error bars for  $c_2$  and  $c_3$  derived using this procedure are given in Table III, together with the best-fit values. Corresponding  $R_2$  values are also listed. Following this procedure, we find error bars of about  $\pm 0.10$  ML for  $c_2$  and  $\pm 0.15$  ML for  $c_3$ .

#### IV. SUMMARY AND CONCLUSIONS

A technique to measure surface structure and chemical composition, with high temporal and spatial resolution, is developed by analyzing LEEM image intensities. Serving as a model system, the surface alloy of submonolayer Pd on the Cu(001) substrate is prepared at 473 K. Structural and compositional information for the first three topmost layers are obtained by a dynamical intensity analysis on a clean Cu(001) surface, a uniform PdCu surface alloy terrace far from the step, and heterogeneous areas near steps at different deposition times. Tests on clean Cu(001) and Cu(001)- $c(2 \times 2)$ -Pd present excellent agreements with previously reported results that show that the reduced data set in LEEM-*IV* presents no limitation to the sensitivity of this technique. Temporal evolution of ultrathin film gives a deposition flux of about 0.9 ML/h, close to the experimental growth rate of 1 ML/h. Step flow is found to be the origin of heterogeneity around steps. Monte Carlo simulations show a well equilibrated surface structure and reproduce the measured concentration profile. Most importantly, this technique has the unique capability to determine surface structural information with high lateral resolution of 8.5 nm.

#### ACKNOWLEDGMENTS

The authors appreciate valuable discussions with Matti Lindroos. This work was supported by the National Science

Foundation under Grant No. DMR-0134933 and the Petroleum Research Fund under Grant No. 46323-AC5. Work performed at Sandia was supported by the U.S. DOE (Office of BES, Division of Materials Science and Engineering). San-

dia is a multiprogram laboratory operated by the Sandia Corporation, a Lockheed Martin Company, for the U.S. DOE's National Nuclear Security Administration under Contract No. DE-AC04-94AL85000.

\*jsun@cisunix.unh.edu

- <sup>1</sup> *Surface Alloys and Alloy Surfaces*, The Chemical Physics of Solid Surfaces Vol. 10, edited by D. P. Woodruff (Elsevier, Amsterdam, 2002).
- <sup>2</sup> J. B. Hannon, J. Sun, K. Pohl, and G. L. Kellogg, *Phys. Rev. Lett.* **96**, 246103 (2006).
- <sup>3</sup> A. R. Koymen, K. H. Lee, G. Yang, K. O. Jensen, and A. H. Weiss, *Phys. Rev. B* **48**, 2020 (1993).
- <sup>4</sup> G. C. Smith, C. Norris, and C. Binns, *Vacuum* **31**, 523 (1981).
- <sup>5</sup> S. H. Lu, Z. Q. Wang, S. C. Wu, C. K. C. Lok, J. Quinn, Y. S. Li, D. Tian, F. Jona, and P. M. Marcus, *Phys. Rev. B* **37**, 4296 (1988).
- <sup>6</sup> T. D. Pope *et al.*, *Surf. Sci.* **337**, 79 (1995).
- <sup>7</sup> P. W. Murray, I. Stensgaard, E. Lægsgaard, and F. Besenbacher, *Surf. Sci.* **365**, 591 (1996).
- <sup>8</sup> J. B. Hannon, H. Ibach, and P. Stoltze, *Surf. Sci.* **355**, 63 (1996).
- <sup>9</sup> C. Barnes, E. AlShamaileh, T. Pitkänen, P. Kaukasoina, and M. Lindroos, *Surf. Sci.* **492**, 55 (2001).
- <sup>10</sup> F. Jona, K. O. Legg, H. D. Shih, D. W. Jepsen, and P. M. Marcus, *Phys. Rev. Lett.* **40**, 1466 (1978).
- <sup>11</sup> S. Crampin and P. J. Rous, *Surf. Sci. Lett.* **244**, L137 (1991).
- <sup>12</sup> E. Bauer, *Rep. Prog. Phys.* **57**, 895 (1994).
- <sup>13</sup> R. M. Tromp, *IBM J. Res. Dev.* **44**, 503 (2000).
- <sup>14</sup> M. Valden, J. Aaltonen, M. Pessa, M. Gleeson, and C. J. Barnes, *Chem. Phys. Lett.* **228**, 519 (1994).
- <sup>15</sup> D. L. Adams, *J. Phys. C* **16**, 6101 (1983).
- <sup>16</sup> D. L. Adams, V. Jensen, X. F. Sun, and J. H. Vollesen, *Phys. Rev. B* **38**, 7913 (1988).
- <sup>17</sup> D. L. Adams, *Surf. Sci.* **519**, 157 (2002).
- <sup>18</sup> J. B. Pendry, *Low-Energy Electron Diffraction* (Academic, London, 1974).
- <sup>19</sup> M. A. Van Hove and S. Y. Tong, *Surface Crystallography by LEED* (Springer Verlag, Berlin, 1979).
- <sup>20</sup> H. Mönig, J. Sun, Y. M. Koroteev, G. Bihlmayer, J. Wells, E. V. Chulkov, K. Pohl, and P. Hofmann, *Phys. Rev. B* **72**, 085410 (2005).
- <sup>21</sup> A. Barbieri and M. A. van Hove, packages available online: <http://www.sitp.lbl.gov/index.php?content=/leedpack/leedpack.html>
- <sup>22</sup> M. A. Van Hove, W. H. Weinberg, and C. M. Chan, *Low-Energy Electron Diffraction* (Springer Verlag, New York, 1986).
- <sup>23</sup> J. E. Demuth, P. M. Marcus, and D. W. Jepsen, *Phys. Rev. B* **11**, 1460 (1975).
- <sup>24</sup> J. R. Noonan, H. L. Davis, and L. H. Jenkins, *J. Vac. Sci. Technol.* **15**, 619 (1978).
- <sup>25</sup> H. L. Davis and J. R. Noonan, *J. Vac. Sci. Technol.* **20**, 842 (1982).
- <sup>26</sup> J. Rundgren, *Phys. Rev. B* **59**, 5106 (1999).
- <sup>27</sup> S. Walter, V. Blum, L. Hammer, S. Müller, K. Heinz, and M. Giesen, *Surf. Sci.* **458**, 155 (2000).
- <sup>28</sup> D. M. Lind, F. B. Dunning, G. K. Walters, and H. L. Davis, *Phys. Rev. B* **35**, 9037 (1987).
- <sup>29</sup> Q. T. Jiang, P. Fenter, and T. Gustafsson, *Phys. Rev. B* **44**, 5773 (1991).
- <sup>30</sup> T. D. Pope, K. Griffiths, and P. R. Norton, *Surf. Sci.* **306**, 294 (1994).
- <sup>31</sup> E. AlShamaileh, C. Barnes, and A. Wander, *J. Phys.: Condens. Matter* **15**, 1879 (2003).
- <sup>32</sup> J. Kudrnovský, S. K. Bose, and V. Drchal, *Phys. Rev. Lett.* **69**, 308 (1992).
- <sup>33</sup> S. V. Eremeev, G. G. Rusina, I. Y. Sklyadneva, S. D. Borisova, and E. V. Chulkov, *Phys. Solid State* **47**, 758 (2005).
- <sup>34</sup> N. Metropolis, A. W. Rosenbluth, M. N. Rosenbluth, A. H. Teller, and E. Teller, *J. Phys. Chem.* **21**, 1087 (1953).
- <sup>35</sup> D. Frenkel and B. Smit, *Understanding Molecular Simulation from Algorithms to Applications* (Academic, San Diego, 2002).